JOURNAL OF GEOPHYSICAL RESEARCH, VOL. 105, NO. B4, PAGES 7945–7960, APRIL 10, 2000

Can a narrow, melt-rich, low-velocity zone of mantle upwelling be hidden beneath the East Pacific Rise? Limits from waveform modeling and the MELT Experiment

Shu-Huei Hung[1] and Donald W. Forsyth

Department of Geological Sciences, Brown University, Providence, Rhode Island

Douglas R. Toomey

Department of Geological Sciences, University of Oregon, Eugene

Abstract. One of the goals of the Mantle Electromagnetic and Tomography (MELT) Experiment is to determine whether a narrow zone of enhanced melt concentration consistent with focused upwelling exists beneath the East Pacific Rise. Using *SKKS*, *sScS*, and *S* phases from two intermediate-depth earthquakes in the Banda Sea and the Tonga-Kermadec region, we demonstrate that there is no positive evidence for the existence of such a zone and that travel time delays for shear waves traveling through it must be <0.5 s. To test whether diffraction and wave front healing could obscure evidence for its existence, we employ a pseudospectral method to simulate finite frequency teleseismic waves propagating through narrow, vertical low-velocity zones. A rich set of reflected, diffracted, and guided waves is generated when *S* waves encounter such a low-velocity channel, particularly at high frequencies. Limiting the frequency content to the lower-frequency bands with good signal-to-noise ratios in the observed phases obscures these waveform complexities. The travel time anomaly is broadened and reduced in amplitude but remains detectable unless the low-velocity zone is very narrow or has only modest velocity contrast. The lower limit of detectability corresponds to a 5-km-wide channel of partial melt extending from 10 to 60 km below the seafloor at the ridge axis with a shear velocity contrast of 0.5 km/s. Although these limits are severe, 3 to 4% melt retention might cause a large enough viscosity reduction and anomalous buoyancy to dynamically focus upwelling into a 5-km-wide channel that falls within the limits. Strongly focused, dynamic upwelling beneath the ridge, however, is probably not compatible with the existence of a broad region of very low shear velocities in the surrounding mantle.

1. Introduction

Oceanic crust is formed within 1-2 km of the spreading center with only minor additions outside this narrow axial zone in the form of seamounts and off-axis lava flows. One of the main questions in mid-ocean ridge dynamics is how magma is produced and then delivered to such a narrow zone. Two end-member scenarios have been developed, both assuming that magma is generated by pressure release, partial melting of upwelling, peridotitic mantle. Passive flow models suggest that the mantle flow pattern is dominantly shaped by viscous drag from rigid spreading plates and predict that the melt is generated in a broad upwelling region that may be >100 km cross. These models require that some mechanism drive or guide the melt laterally toward the ridge [e.g., *Spiegelman and McKenzie*, 1987; *Phipps Morgan*, 1987; *Sparks and Parmentier*, 1991]. Melt concentrations may be low, perhaps <1%, throughout the entire melt production region if melt is efficiently extracted by porous flow. In the second scenario, very low viscosity in the melting regime combined with buoyancy from mantle depletion and melt retention force a focused upwelling that may be as narrow as a few kilometers wide [e.g., *Buck and Su*, 1989; *Scott and Stevenson*, 1989]. Melt transport then can be primarily vertical, driven simply by its buoyancy. In these

[1]Now at Department of Geosciences, Princeton University, Princeton, New Jersey

Copyright 2000 by the American Geophysical Union.

Paper number 1999JB900316.
0148-0227/00/1999JB900316$09.00

dynamic flow models, melt retention of at least several percent is required to provide buoyancy and to reduce the viscosity [*Hirth and Kohlstedt*, 1995a]; otherwise, focusing will not occur at fast spreading rates [*Cordery and Phipps Morgan*, 1993]. Dynamic flow models thus predict a narrow zone of relatively high melt concentration extending tens of kilometers vertically beneath spreading centers.

One of the primary goals of the Mantle Electromagnetic and Tomography (MELT) Experiment is to distinguish between these two scenarios of upwelling by searching for the existence of a narrow zone of anomalously low seismic velocities beneath the fast spreading East Pacific Rise that would be expected if there is a region of rapid upwelling and high melt concentration. Beginning in November 1995, 51 ocean bottom seismometers (OBSs) were deployed for a period of 6 to 7 months in an array (Figure 1) across the southern East Pacific Rise (EPR) to record teleseismic earthquakes [*Forsyth et al.*, 1998a]. Analyses of the P and S wave delays, phase velocities of Rayleigh waves, and waveforms of regional events showed that melt is probably present to a depth exceeding 100 km in a broad region, several hundred kilometers across [*Toomey et al.*, 1998; *Forsyth et al.*, 1998b; *Webb and Forsyth*, 1998]. There is no indication in the pattern of body wave delays for the presence of a narrow, low-velocity melt conduit extending tens of kilometers into the mantle beneath the spreading center [*Toomey et al.*, 1998; *Forsyth et al.*, 1998a].

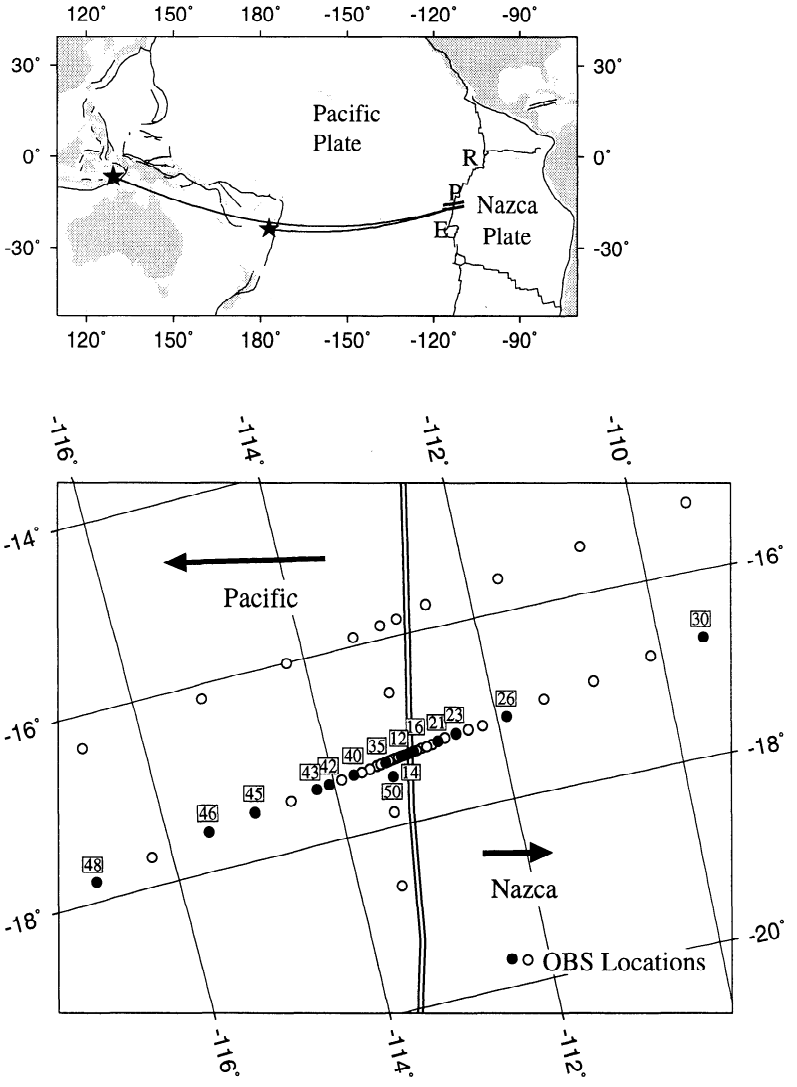

Figure 1. (top) The locations of the Banda Sea and Tonga earthquakes denoted by stars and their great circle ray paths to the MELT OBS arrays across the East Pacific Rise (EPR) shown by the two solid lines. (bottom) Deployment sites of 51 ocean bottom seismometers of the MELT Experiment area. Projection is about the pole of relative plate motion between the Pacific and Nazca plates. The solid symbols are the numbered stations that recorded shear waveforms used in this study. Arrows indicate the absolute plate motion vectors, which differ from the relative plate motion by <2° in this area.

There is some concern, however, that a narrow zone might be hidden by the effects of finite frequency wave propagation and the limits of resolution. When incoming wave fields propagate through local heterogeneities, they are distorted in a complex way due to energy scattering and diffraction, especially when the heterogeneities vary on spatial scales of the same order as the Fresnel zone of the passing wave fronts [*Nolet and Moser*, 1993; *Gudmundsson*, 1996]. The perturbed wave fronts, carrying the information of the scale and intensity of velocity anomalies, are smoothed to some extent as they proceed to the surface. This so-called wave front healing effect may erase the time delay formed earlier in a low-velocity zone [*Gudmundsson*, 1996]. The shortest-period P and S waves detected from teleseismic events in the MELT Experiment were 2-3 s for P waves and about 6 s for S waves, corresponding to minimum wavelengths of about 25 km, which is equal to or greater than the expected width of a dynamically focused upwelling zone.

The purpose of this paper is to explore limits on the properties of a melt-rich conduit that could remain hidden in the MELT Experiment data. Obviously, as the width or velocity contrast of such a conduit approaches zero, it will become undetectable. By generating synthetic seismograms with numerical formulations of three-dimensional (3-D) wave propagation that incorporate all the effects of diffraction, mode conversions, and finite wavelength in a realistic geometry, we can better understand the limits of resolution of the existing data set. We find that any vertical melt channel beneath the array must either be extremely narrow or have quite a subtle velocity contrast with the surrounding asthenosphere. The limits, however, are just loose enough that it is possible that enough melt is present in a channel to make dynamic concentration of upwelling feasible while still avoiding detection.

2. Observations

Toomey et al. [1998] reported on 500 P and S wave relative delay times from 20 teleseismic earthquakes observed at the array. Altogether 51 OBSs were deployed, but at some stations, only pressure variations were recorded on differential pressure gauges (DPGs). P waves were recorded on the DPGs, but good signal-to-noise ratio records at frequencies higher than 0.1 Hz were obtained only on the three-component seismometers. P and S wave delays were thus measured only at 24 sites with functioning seismometers. Orientation of the horizontal components was determined by the polarization of long-period Love and Rayleigh waves from many events and is accurate to $\sim 5^\circ$. The only evidence for a narrow zone of partial melt was a 0.3 to 0.4 s delay for P waves at the station directly at the ridge axis relative to a site 6 km off axis [*Toomey et al.*, 1998]. Because this delay was observed at no other site, it was attributed to magma in the crust or immediately beneath the Moho at the ridge axis [*Forsyth et al.*, 1998a]. Slanting rays from earthquakes in the western Pacific or beneath South America recorded at other sites would have intercepted the source of this anomaly if it extended more than a few kilometers into the mantle.

In this paper we use the teleseismic S waveforms with the highest resolvable frequencies recorded during the experiment, which are the phases most likely to reveal the existence of a narrow low-velocity zone from travel time delays and waveform variations. We concentrate on two intermediate-depth earthquakes with large magnitudes and decent signal-to-noise ratios, occuring on April 16, 1996, in the Tonga-Kermadec subduction zone at a depth of 111 km ($m_b = 6.4$) , and on December 25, 1995 in the Banda Sea at a depth of 150 km ($m_b = 6.2$) (Figure 1). The Tonga event has a simple source-time function and generates clean and coherent shear waveforms at frequencies up to 0.15 Hz (Figure 2). We filter the seismograms using a fourth-order, causal Butterworth filter between 0.03 and 0.15 Hz to optimize the signal-to-noise ratio; the dominant period of the phase pulses is 10 to 14 s and the cleanest phases are S and $sScS$. S comprises roughly equal SV and SH recorded on the radial and transverse components, while $sScS$ is dominantly transverse. The waveforms from the Banda Sea event contain higher-frequency spectra, and the recorded $SKKS$ phases centered at the period of $\sim$6 to 7 s can be coherently identified when the seismograms are band-passed between 0.04 and 0.2 Hz (Figure 3), though the signal-to-noise ratio is lower than the Tonga event. The great circle paths from these two earthquakes to the OBSs lie nearly along the primary linear array, so the azimuths of the rays leaving the source vary by only 1.5° from the western to the eastern end of the array. The $sScS$ and $SKKS$ arrivals nominally approach the array at nearly identical azimuths and incidence angles. At epicentral distances of $\sim 60^\circ$ for the Tonga event and 145° for the Banda Sea event to the center of the array, the angle of incidence in the shallow upper mantle is $\sim 29^\circ$ for S waves and 16° for $sScS$ and $SKKS$.

There is no significant difference in waveforms of S and $sScS$ phases on the transverse component from the farthest off-axis stations, S48 on the Pacific plate and S30 on the Nazca plate, to S14, the station 6 km to the east of the axis. S14 was the closest station to the spreading center for the Tonga event because at this late point in the deployment, the axial station was no longer working (Figure 2). More functional seismometers recorded the earlier Banda Sea event, including the rise axis station S12 (Figure 3). There is also no clear evidence for a narrow, low-velocity zone from changes of amplitude and waveform shape in the radial $SKKS$ phase. However, shear wave splitting is evident from unambiguous transverse energy for $SKKS$ (Figure 3b). In an isotropic, layered medium, $SKKS$ should have only radial energy. Note that the amplitudes of the transverse $SKKS$ phases tend to be larger relative to the radial component on stations 40 through 48 compared

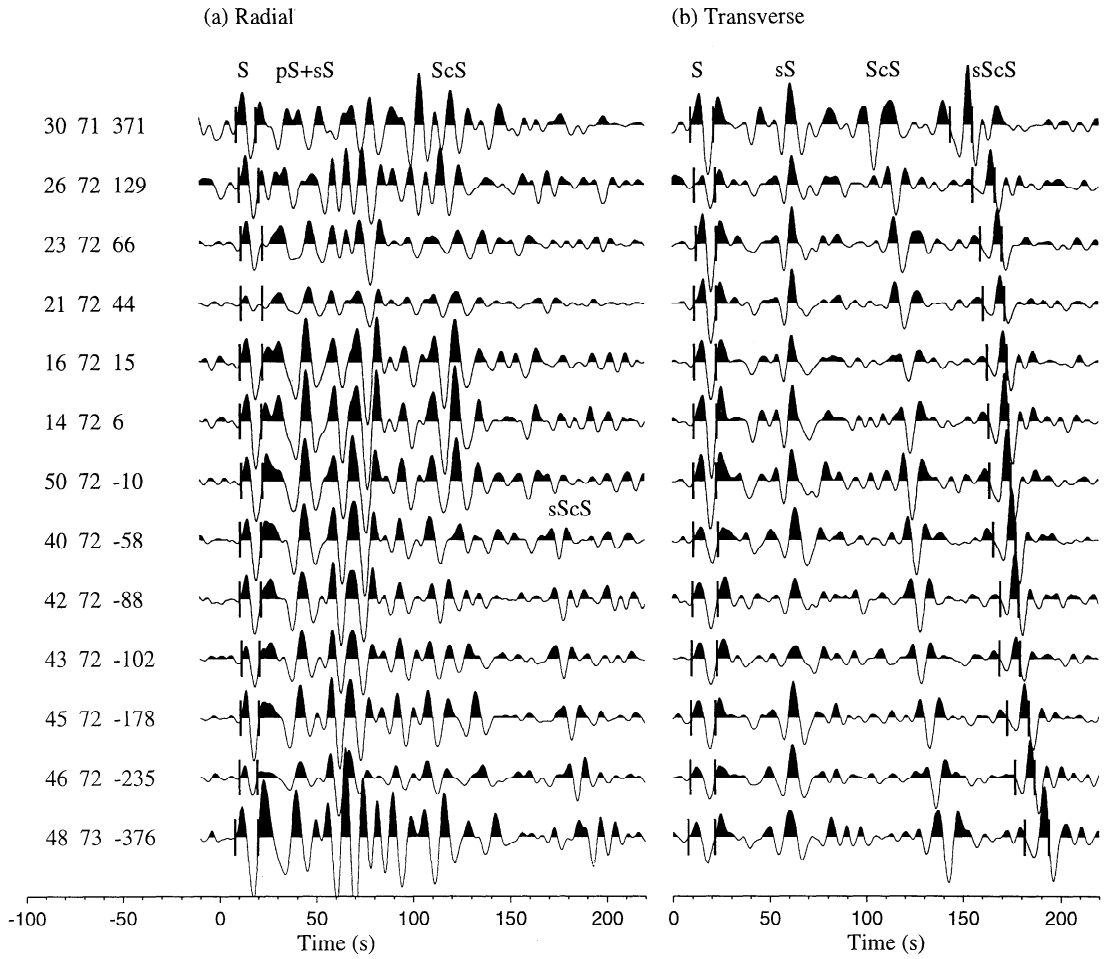

Figure 2. Shear waveforms recorded at the MELT OBS array from the Tonga event. The seismograms are rotated to the radial and transverse azimuths and filtered between 0.03 and 0.15 Hz. Each seismic trace has been shifted so that time $t = 0$ corresponds to the S phase arrival predicted from the IASPEI91 model. Labels indicate station number, back azimuth (degrees), and cross-axis distance (km) from the ridge with negative values to the west on the Pacific plate. A sequence of clear and coherent S, sS, ScS, and $sScS$ arrivals is shown on the transverse component across the array. Although the variation of the waveforms on the radial component is less coherent due to SP conversions and water reverberations, the wave shape of the direct S phase is very similar across the array. The $sScS$ phase is nearly transversely polarized but appears with increasing amplitude on the radial component to the west of the ridge axis. The short vertical bars indicate the time windows used for relative cross-correlation travel time measurement.

to other stations, in accord with the observation that shear wave splitting times are nearly twice as large to the west of the East Pacific Rise as to the east [*Wolfe and Solomon*, 1998]. Seismic anisotropy is probably also the cause of the elliptical particle motions of S arrivals from the Tonga event. Because most of the SV energy of $sScS$ is lost in conversions to P energy both at the seafloor and at the core-mantle boundary, $sScS$ is expected to be observed primarily on the transverse component. The striking differences across the array of amplitudes of $sScS$ phases on the radial component, which only appear at the stations on the Pacific plate, are probably caused by variations in the strength of shear wave anisotropy or amount of splitting times. To measure the relative S, $sScS$, and $SKKS$ delays on both the components, we use the IASPEI91 model [*Kennett and Engdahl*, 1991] to remove the predicted moveout and cross correlate the first complete cycle of the waveforms between the stations using the technique from *VanDecar and Crosson* [1990]. Because the waveforms used for cross correlation are very similar across the array, the estimated relative delays are not sensitive to the chosen window length and filter.

The cross-axis variation in the relative S travel times displays a broad delay gradually decreasing with distance from the ridge, but there is no peaked, slow anomaly near the axis (Figure 4a). Seismic anisotropy probably has a substantial influence on the phase delays, as indicated by the discrepancy in differential times between the radial and transverse components. The variation of the $sScS$ delay is more subdued with only ~1.5 s difference from the slowest to the fastest

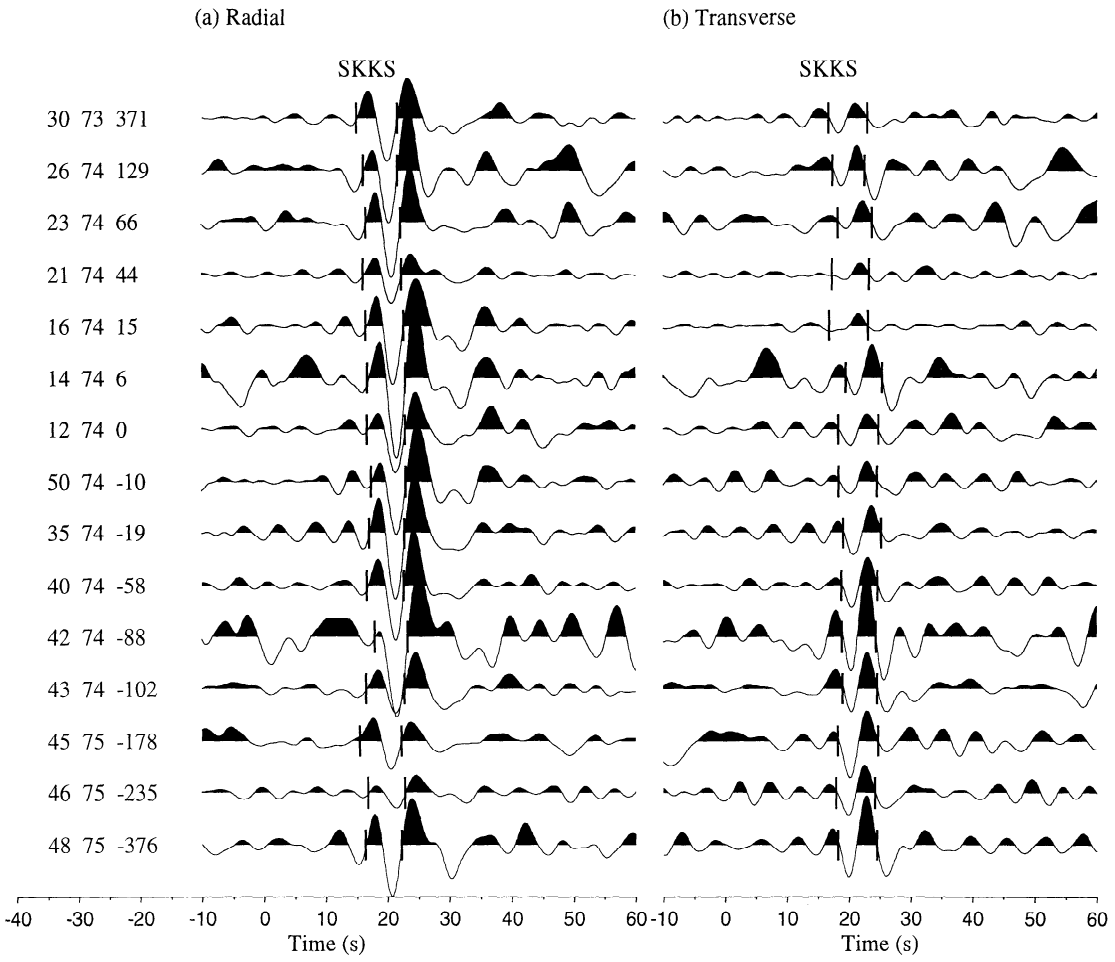

Figure 3. *SKKS* waveforms recorded at the MELT OBS array from the Banda Sea event. The seismograms are rotated to the radial and transverse azimuths and filtered between 0.04 and 0.2 Hz. Each seismic trace has been shifted so that time $t = 0$ corresponds to the *SKKS* phase arrival predicted from IASPEI91 model. The appearance of transverse energy for the radially polarized *SKKS* is indicative of shear wave splitting. See Figure 2 for explanation of labels.

arrival and smoother variations from station to station; again, there is no narrow peak in delays that might indicate the presence of a few kilometer-wide low-velocity zone (Figure 4b). There is asymmetry in the delays with slower arrivals to the west, in agreement with the asymmetry observed in the phase velocity of Rayleigh waves [*Forsyth et al.*, 1998b] and the average P and S wave delays from 20 sources [*Toomey et al.*, 1998].

The delays of the *SKKS* phases from the Banda Sea event have larger uncertainties, particularly on the transverse component, which has a lower signal-to-noise ratio. Arriving with the same azimuth and incidence angle as those of *sScS* phase, the radial *SKKS* (Figure 4c) also shows more asymmetric variation in delay than S (Figure 4a), which has a shallower incidence angle. There appears to be a step change with a 0.5 to 1 s delay on the rise axis station relative to the station 20 km off axis to the east. However, we also observe no peaks in delay near the axis. The contrast in delay pattern between the S and *sScS* or *SKKS* phases may also be attributable to anisotropy; the P wave delay pattern for events at similar azimuths but with different angles of incidence varies in a fashion that is consistent with a more vertical alignment of the olivine a axis near the ridge [*Toomey et al.*, 1998].

Seismic anisotropy under the array has been detected from shear wave splitting of *SKS* and *SKKS* phases as well as azimuthal dependence of phase velocity in Rayleigh waves [*Wolfe and Solomon*, 1998; *Forsyth et al.*, 1998b]. Both of these studies found that the fast polarization azimuth lies approximately parallel to the absolute plate motion direction or to the direction of spreading, which are indistinguishable in this area. Splitting is nearly a factor of 2 greater beneath the Pacific plate than beneath the Nazca plate, which is consistent with our observation that the largest radial components generated by the dominantly transverse *sScS* are found to the west of the axis. Because the separation of two split shear waves strongly depends on the propagation direction, the S and *sScS* phases may split into quasi-shear phases with unequal splitting delays. Interference between the split phases on paths that do not lie along

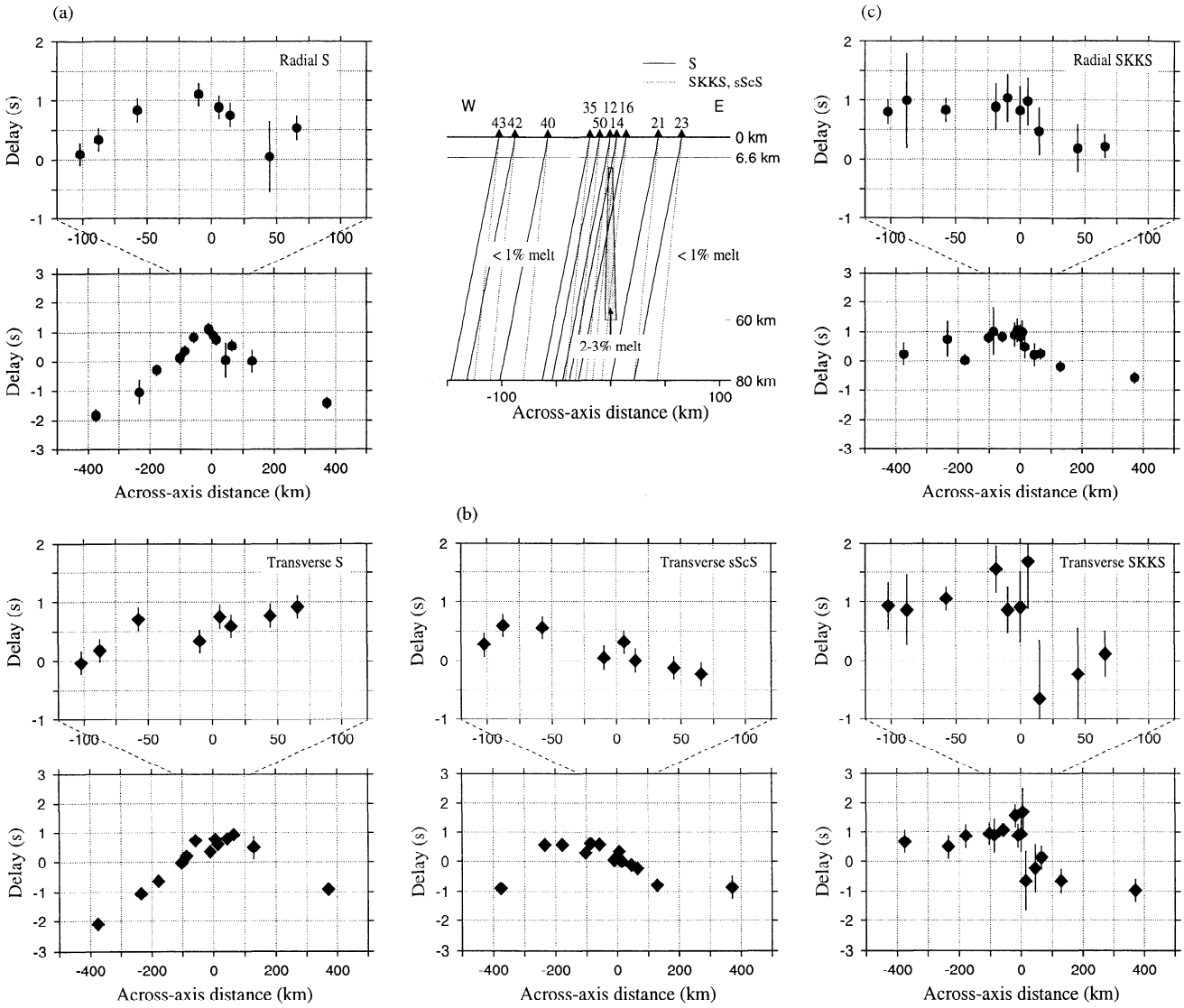

Figure 4. Cross-axis variations of the shear wave delays on the radial and transverse components for the (a) *S* and (b) *sScS* phases from the Tonga event and (c) the *SKKS* phases from the Banda Sea event. Time segments used for cross correlation are indicated by vertical bars on the seismograms in Figures 2 and 3. Inset shows geometry of a narrow (~4-10 km wide), melt-rich conduit extending to a depth of 60 km hypothesized to explain the axial topographic high along the East Pacific Rise [*Magde et al.*, 1995]. Solid and dotted lines depict slanting rays of teleseismic *S*, *sScS*, and *SKKS* phases from earthquakes in the western Pacific that may intercept the axial anomaly and arrive at the recording MELT OBS stations.

symmetry axes can change the waveforms and potentially mask the signal caused by heterogeneity. To insure that we are not missing a ridge axis signal, we need to take into account the effects of anisotropy.

Unlike the *SKKS* splitting which is simply attributed to the receiver-side anisotropy, it is not obvious how to best correct shear wave splitting imparted on the *S* and *sScS* arrivals which accumulate the effects of both source- and receiver-side upper mantle anisotropy as well as a potential contribution from the core-mantle boundary region (D") for *sScS*. Potentially, the splitting of the *S* phases also can be very different from the *SKKS* phases because they have a shallower angle of incidence. Beneath the axis where the preferential orientation of olivine is expected to change rapidly as the flow changes from vertical upwelling to horizontal, the difference in incidence angle could be a particular problem. Although the effects of multiple anisotropic layers can be quite complicated [*Wolfe and Silver*, 1998], the simplicity of the waveforms suggests that we would be unable to unravel anything more complex than simple splitting parameters. We therefore use the procedure of *Silver and Chan* [1991] to extract the polarization direction ϕ of leading shear waves and the delay δt between fast and slow arrivals that yield the most linear particle motion. We find that the splitting parameters deter-

mined solely by the linearity of shear wave polarization are poorly constrained, as is often the case with single arrivals [*Wolfe and Silver*, 1998]. Considering that *SKS* and *SKKS* splitting, splitting of *S* waves from local earthquakes [*Hung and Forsyth*, 1999], and Rayleigh wave azimuthal anisotropy all show a coherent fast direction under the array approximately perpendicular to the ridge, we add this prior information to the splitting inversion to place a more solid bound on the resolved fast direction and delay. We create an a priori error surface that assumes a normal distribution centered at (1.5 s, N78°W) for δt and ϕ with the 95% confidence errors (0.5 s, 10°), based on the average splitting time for *SKS* phases. The final splitting parameters for the *S* and *sScS* waves are individually measured by stacking the a priori constraint with the solution from linearization of particle motions of the phases themselves. The resulting splitting times and fast directions are similar to those from *SKS* and *SKKS* splitting [*Wolfe and Solomon*, 1998]; the particle motions for *S* and *sScS* phases do not require an additional component of splitting generated elsewhere along the path.

To check that shear wave splitting has not obscured a ridge axis signal, we rotate each of the shear phases into the fast and slow directions determined by *Wolfe and Solomon* [1998]. Figure 5a shows the delays of components of the *S* phases of the Tonga event in the fast and slow directions. The variation on the fast component is very similar to that for the radial *S* phase, except for station S21 40 km east of the axis that has little radi-

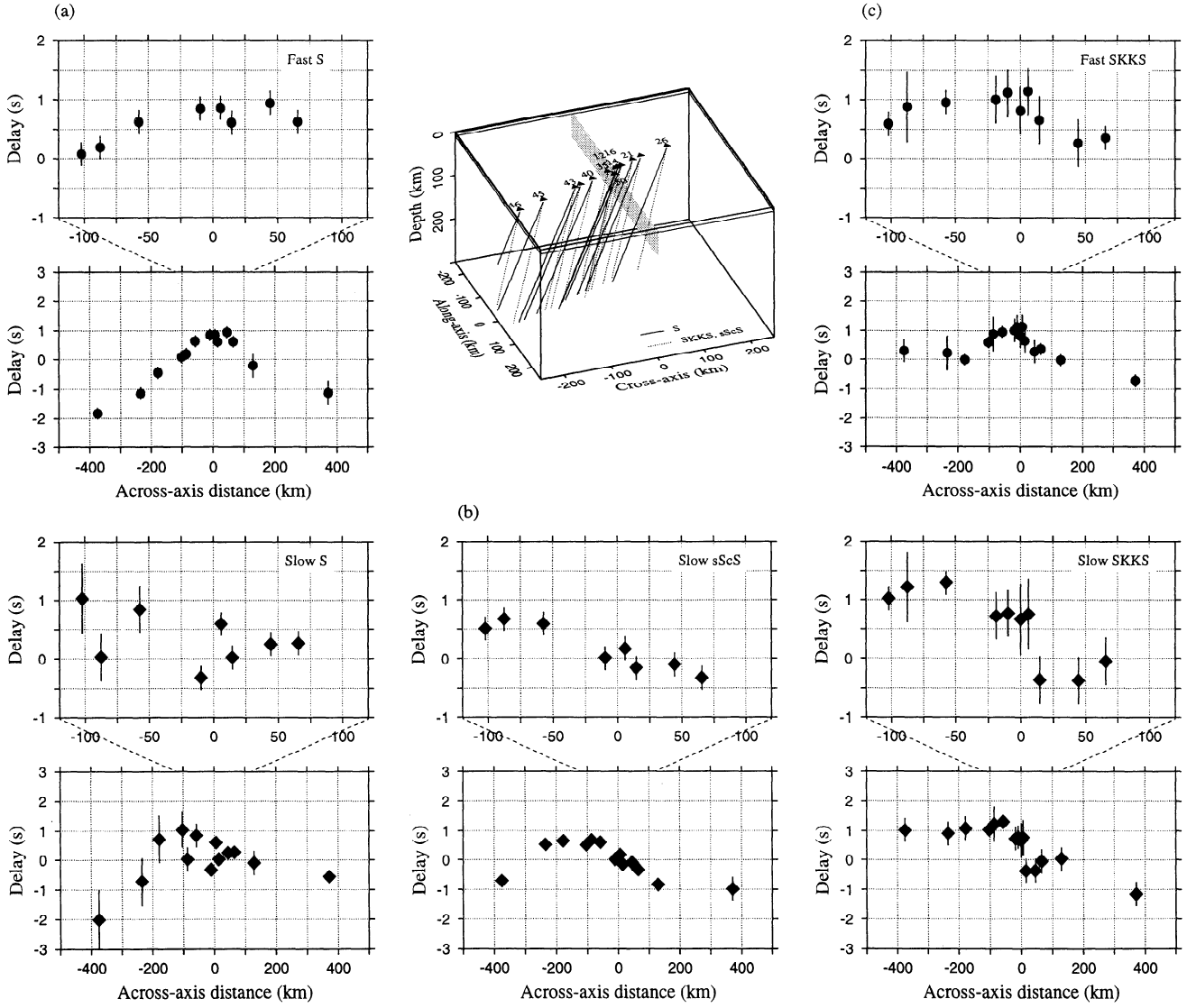

Figure 5. Cross-axis variations of the shear wave delays on the fast and slow components for the (a) *S* and (b) *sScS* phases from the Tonga event and (c) the *SKKS* phases from the Banda Sea event. Inset shows the 3-D model configuration, OBS locations, and geometrical ray paths of simulated incoming *S*, *sScS*, and *SKKS* phases in waveform modeling. A shaded 2-D rectangular cross section indicates a symmetric, 4-km-wide, low-velocity zone embedded beneath the axis at depths of 10-60 km below the seafloor.

al energy and was assigned a large uncertainty (Figure 4a). The S waves from this event have little energy in the slow directions and therefore were assigned large errors, particularly to the west of the ridge axis. The split *sScS* phases are mostly polarized in the slow direction, and the delays derived from the slow component are virtually unchanged from the original pattern observed on the transverse component (Figure 5b). The delay patterns of the fast and slow *SKKS* arrivals are similar to those on the radial and transverse components with no narrow peak but a steep gradient from the axis to the east (Figure 5c). We measure the *SKKS* delays at different narrow frequency bands between 5 and 40 s, and the step-like variation in the delays appears to be less pronounced at longer periods. Finite frequency wave diffraction renders travel time measurements sensitive to the periods of waveforms for cross correlation, particularly when the scale of velocity heterogeneity is the same as or smaller than the seismic wavelength [e.g., *Gudmundsson*, 1996]. Such frequency-dependent delays suggest that there might be a rapid change of shear wave velocity on a scale of a few tens of kilometers, although there is no strong indication in either the *S*, *sScS*, or *SKKS* anisotropy-corrected delays of a narrow peaked anomaly near the axis. Instead, we observe a broad anomaly, slower on the west of the ridge axis, and a rapid increase in the S wave velocity to the east. These patterns are both in agreement with other types of observations of asymmetry [*Forsyth et al.*, 1998a]. Any axial anomaly must be smaller than ~0.5 s to yield such a broad delay pattern. The question then becomes whether this level of uncertainty could hide a narrow upwelling region with low shear wave velocities.

3. Waveform Modeling

To address the question of the size and shape of the travel time anomaly and the nature of any waveform changes that might be expected for an axial low-velocity zone, we perform numerical simulations of finite frequency seismic waves propagating through postulated heterogeneities. We do not expect to fit the observed waveforms exactly; instead, we are more concerned to know how much of the travel time information from a wave front distorted by a deep-seated structure will remain at the surface and be captured by the MELT array. We will demonstrate that some highly diagnostic waveform perturbations can be generated by moderate axial anomalies at frequencies between 0.25 and 0.4 Hz. These perturbations are lost in the frequency range that we can observe from the *S*, *sScS*, and *SKKS* phases, but the travel time anomalies are not.

We represent the hypothetical upwelling zone as a simple, symmetric, 2-D structure of rectangular cross section embedded beneath the ridge (see Figures 4 and 5), although some three dimensionality beneath the EPR is suggested by the Rayleigh wave tomography, P and S delays, and minor, along-axis variations in topography and gravity anomaly [*Forsyth et al.*, 1998b; *Toomey et al.*, 1998; *Scheirer et al.*, 1998]. The geometry of the melt pockets in the narrow, partial melting region is assumed to be randomly oriented thin films that produce no anisotropy. Therefore only the shear modulus is affected by the melt concentration, and the velocity reduction in the S wave due to the presence of melt is more pronounced than in the P wave. In our modeling, the velocity contrasts between the low-velocity zone and the surrounding mantle are 1.0 km/s for the S wave and 0.77 km/s for the P wave. This velocity reduction for the S wave is approximately the difference in S velocity between old oceanic lithosphere at a depth of 50 km and the asthenosphere in the vicinity of the ridge axis at the same depth [*Nishimura and Forsyth*, 1989; *Webb and Forsyth*, 1998], a difference that may be created by the presence of 1 to 2% melt in pockets with aspect ratio of the order of 0.01 [*Forsyth*, 1992]. Several percent melt could be present with the same S velocity anomaly if the aspect ratio is larger; in that case the P wave anomaly would be increased.

The method we use for full waveform modeling is a three-dimensional, multidomain, pseudospectral scheme that employs different grid spacing in each domain to efficiently calculate the wave fields in an elastic medium overlain by an acoustic layer [*Hung and Forsyth*, 1998]. This approach is particularly suited to modeling waveforms recorded on the seafloor that are affected by water reverberations. Wave fields and the structure are described by global basis functions, Fourier series in the horizontal directions, and Chebyshev polynomials in the vertical direction, while time derivatives are calculated by finite differences. Use of global basis functions instead of finite differences minimizes numerical inaccuracies such as grid dispersion and artificial anisotropy. The horizontal grid spacing is uniform, set at 2 km, but the vertical mesh has finer spacing near the boundary between domains and in the slow water layer. The model space is divided into two domains: the 3-km-thick water layer, and the elastic domain including a 6.6-km-thick crust and a uniform velocity upper mantle layer extending down to 300 km. An incoming teleseismic wave is simulated by introducing an initial condition of a spatial disturbance in velocity that is in phase along planes perpendicular to a ray with azimuth and incidence angle duplicating that predicted for teleseismic S or *sScS* arrival from the Tonga event or *SKKS* from the Banda Sea event. The coordinate system is based on ridge geometry, with the axis of the ridge along one horizontal axis. Though the velocity structure is two-dimensional, the wave vector or the normal to the plane wave for an incoming shear phase is not vertically incident, and its azimuth is oblique to the ridge axis. Because the initial particle velocity prescribed on the planar wave fields varies along the ridge axis, three-dimensional simulation of wave propagation is required in the waveform modeling. The SV polarization direction is defined as the vector orthogonal to the wave

vector on the vertical plane containing the wave vector, while the *SH* is in and out of this vertical plane. At time $t = 0$ the spatial variation in particle velocity for a given polarized wave along its polarization direction is described by the first derivative of a Gaussian curve (equivalent to a Ricker wavelet in acceleration) with variance $\sigma^2 = \lambda^2/8\pi^2$, which yields an equivalent source pulse with a characteristic period of order λ/c and centroid of angular frequency, $\sqrt{2}(2\pi c/\lambda)$, where c is the mantle shear wave velocity (Plate 1a). Choosing $\lambda = 18$ km yields an oscillation just at the limit of resolution given our grid spacing. Worried about possible aliasing, we doubled the density of grid points in a test calculation and found no significant change in the waveforms.

As time proceeds in the numerical experiment, the disturbance propagates away in both directions normal to the initial plane (Plate 1b). At the bottom and sides of the model region we employ attenuating strips that absorb the outgoing waves. Small artificial reflections are generated at the sides, but these arrive at the surface late enough in the area of interest that they do not interfere with the waveform of interest. Details of the numerical methods are described by *Hung and Forsyth* [1998]. Upon arrival of the wave at the crustal layer or axial heterogeneity, reflections and mode conversions take place (Plates 1c and 1d). We ignore differential attenuation between the low-velocity region and the surroundings because path lengths within the melting region are short; at the periods and wavelengths involved

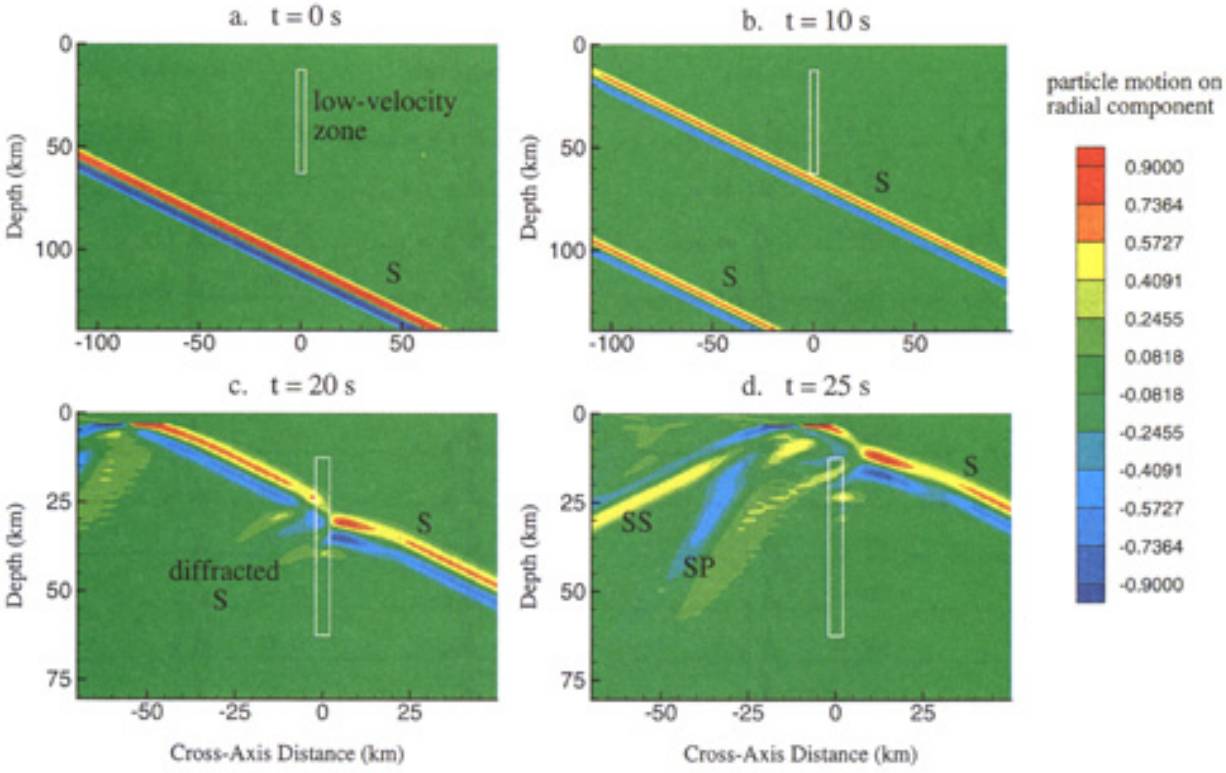

Plate 1. A sequence of S wave fields showing the radial component from a simulation of seismic wave propagation through a subaxial low-velocity anomaly. The azimuth and incident angle of the normal to the plane wave are 60° clockwise from the ridge axis and 29°, respectively. The snapshots are shown on the vertical plane normal to the ridge axis with zero at the axis for the radial component, although calculations are three-dimensional. Four time frames are shown at $t = 0$, 10, 20, 25 s after initiating the wave front that simulates the teleseismic S arrival from the Tonga event. The model space includes a 3-km water layer overlying a 6.6-km oceanic crust and homogeneous mantle except that a low-velocity channel with a width of 12 km is embedded between 10 and 60 km beneath the axis. (a) Initial velocity perturbation. (b) Plane waves propagating away from the initial disturbance and the upgoing wave front approaching a narrow, subaxial low-velocity zone. (c and d) Close views of near-axis wave fields affected by the low-velocity channel. In Plate 1c, the planar wave front is distorted from interaction with the slow anomaly. Diffracted S waves yield a secondary hyperbola-curved wave front guided up the channel. Plate 1d shows the complex energy interference of multiple reflected and converted waves from the water and crustal layers and the subaxial heterogeneity after the initial wave front passes through the channel. The P and S waves reflected at a combination of the Moho and seafloor can be seen.

in this study, attenuation effects are likely to be negligible. The extent of our model is asymmetric about the axis to allow for the horizontal component of propagation of the incoming wave and for reverberations in the crustal and water layers to build up to approximately equilibrium levels. To reduce the computational cost, we confine our attention to distances of 200 km or less from the axis. Synthetic seismograms can be retained for any grid point within the medium. We chose to generate synthetic record sections by selecting grid points closest to the stations of the array.

We tried several models that vary the width of the melt conduit from 4 to 12 km and with vertical extent either from 10 to 60 beneath the seafloor or from 30 to 60 km. We trace the whole wave fields initially coming in at ~60° from the strike of the ridge axis (or N255°E) with two different incident angles, 29° and 16° corresponding to the recorded S and $sScS$ or $SKKS$ phases, respectively. Figures 6 and 7 compare the waveforms from plane waves incident with the two different angles for the case of a 4-km-wide low-velocity zone extending from 10 to 60 km. At distances >30 or 40 km from the axis, the transverse and radial waveforms are very simple and nearly undisturbed by the presence of an axial velocity anomaly. At closer distances, there are pronounced changes in waveform. On the side nearer the source, the initial pulse remains nearly unchanged, but there are distinct reflections from the melt column that are particularly strong on the radial component (Figure 6a). On the far side of the axis, where the direct path

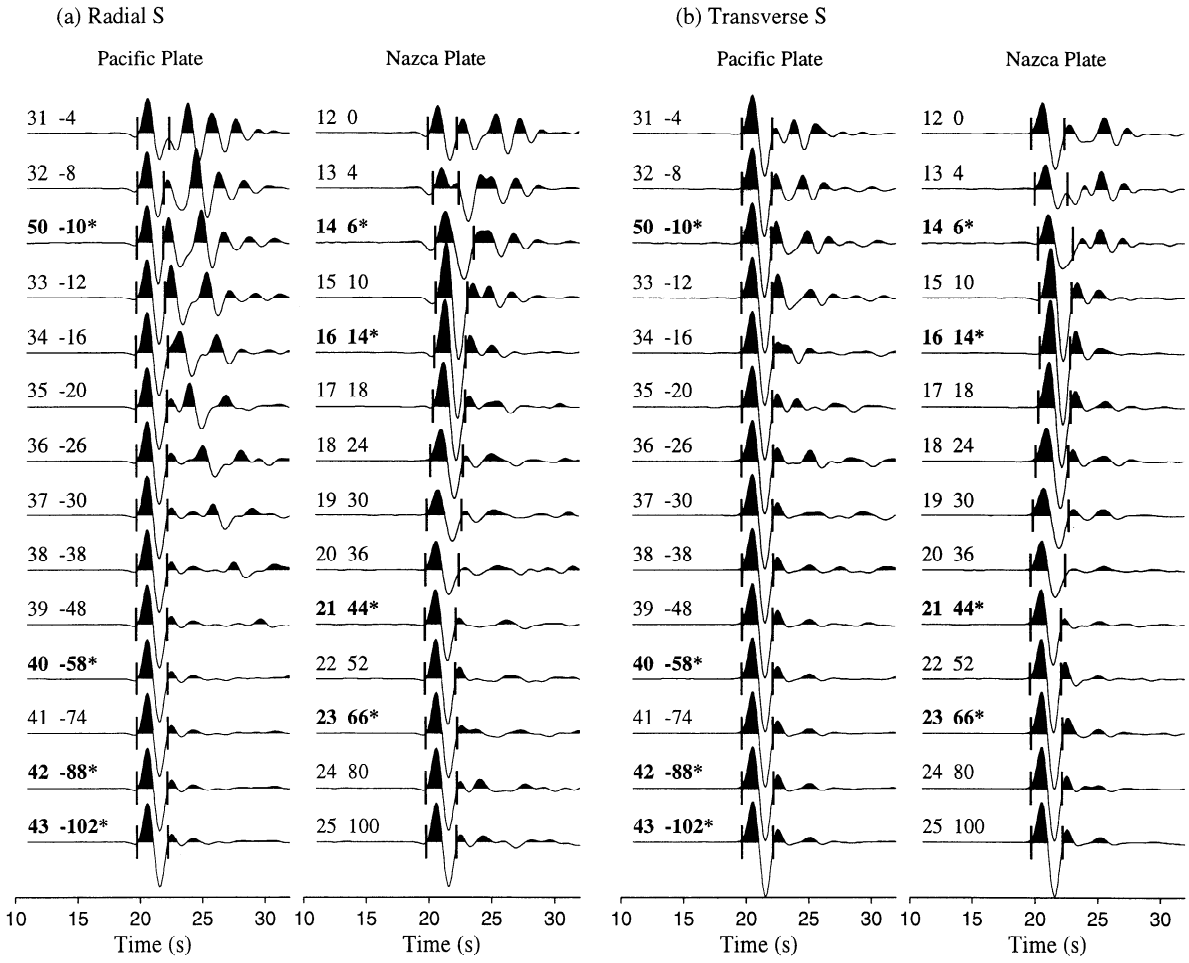

Figure 6. Synthetic seismograms on the (a) radial and (b) transverse components with cross-axis distances <200 km. The waveform modeling simulates an incoming S waves with an incidence angle of 29° and azimuth of 60° from the ridge axis, passing through a 4-km-wide, low-velocity melt channel (strike 0°, dip 90°) embedded beneath the axis at depths of 10-60 km. Labels denote the station number and cross-axis distance (km) from the ridge axis with asterisks indicating the OBSs that recorded data during the experiment. The waveforms have the same frequency content as the imposed plane wave front with a dominant period of about 2.5 s. The waveforms show diagnostic variations across the array on all three components, particularly on the radial components of the stations to the west where large-amplitude second and third phases reflected off the front and back edges of the melt column interfere with first arrivals. The wave front guided up the low-velocity channel arrives late directly above or near the axis to the east.

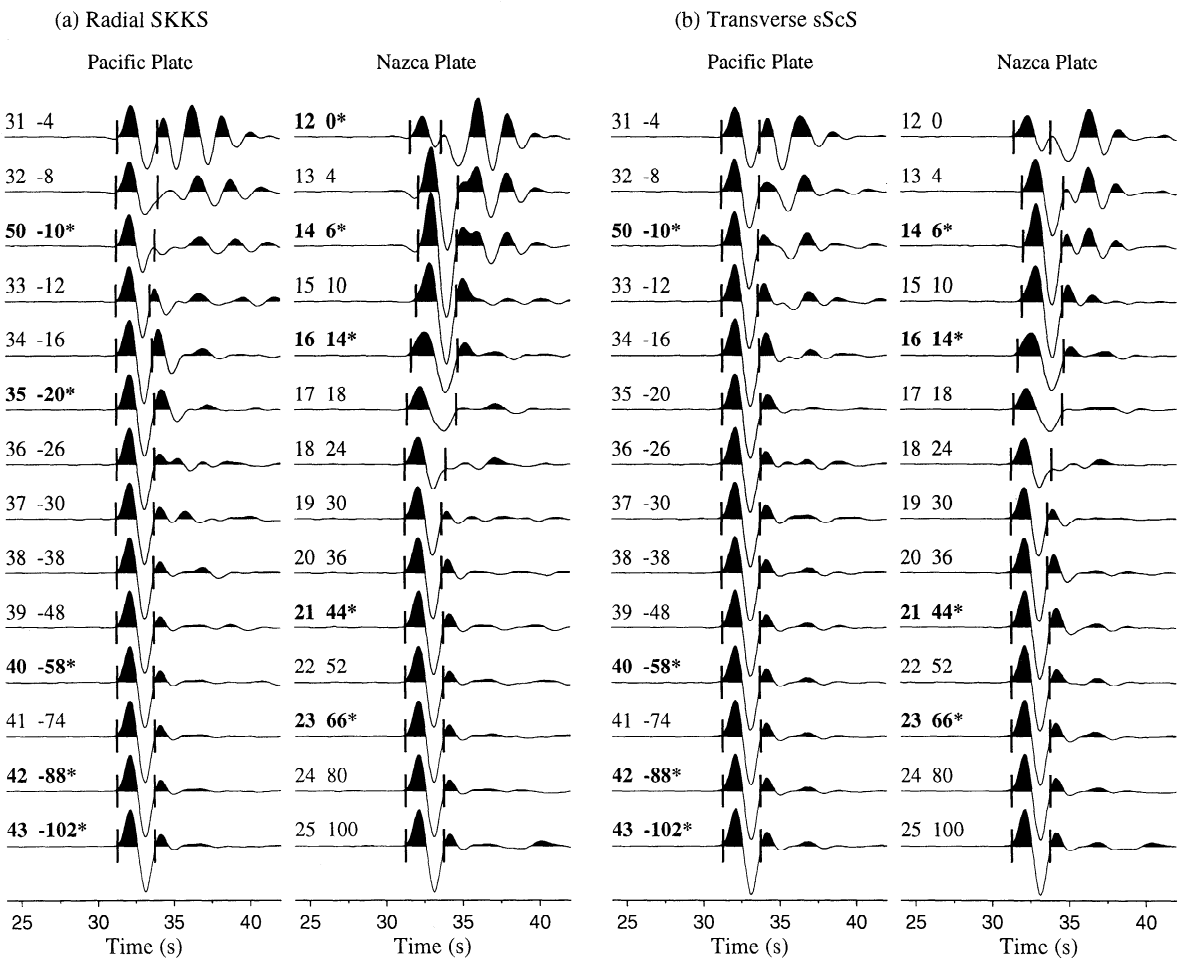

Figure 7. Synthetic waveforms for (a) the radial *SKKS* phases from the Banda Sea event and (b) the transverse *sScS* phases from the Tonga event. The angle of incidence is 16°. See Figure 6 for detailed descriptions of the labels and velocity model. Waveforms are significantly different from the S wave. The phases reflected off the melt column arrive closer to the first arrivals and are captured at nearer-axis stations than the S arrivals. The guided waves propagating upward to the axial stations are clearly shown on the transverse *sScS* at stations S12, S13, and S14.

rays pass through or near the anomalous region, there are changes in waveform and amplitude of the initial phase. Sites directly above or very near the axis are affected by a wave that seems to be guided up the low-velocity channel. Note particularly the simple, second phase on the transverse component at site 12 (Figure 6b). The complicated waveforms at higher frequency would provide more information about the details of the structure, such as the sharpness of the velocity change across the edge of the low-velocity zone. Reflected phases are less prominent on the radial *SKKS* and transverse *sScS* simulations with their more vertical angle of incidence (Figures 7a and 7b). Large secondary phases are confined to within ~10 km of the axis, but significant changes in waveform continue out to ~25 km, beyond the distance where a direct ray would encounter the anomaly.

The maximum predicted delay times are not very sensitive to the change of incidence angles. We measure delay times in the same way that it is done with the real observations. We subtract the predicted moveout for the incoming plane wave and window the first cycle of the characteristic waveforms for interstation cross correlation. Because the waveforms change near the axis, the apparent delay is somewhat sensitive to the length of the window chosen for the cross-correlating phase but by duplicating the usual procedure for signals in the presence of noise [e.g., *Toomey et al.*, 1998], the delays are representative of what would be found in a typical observational study. For both phases we predict a spike-shaped pattern with the maximum delay close to 1 s for these three phases (Figure 8a). The mode conversion that produces a P wave precursor preceding the direct shear arrival substantially affects the waveform shape on the vertical component, causing earlier arrivals and somewhat different delay patterns from the two horizontal components. The slowest arrival for the S wave should be at station 14, ~6 km east of the axis.

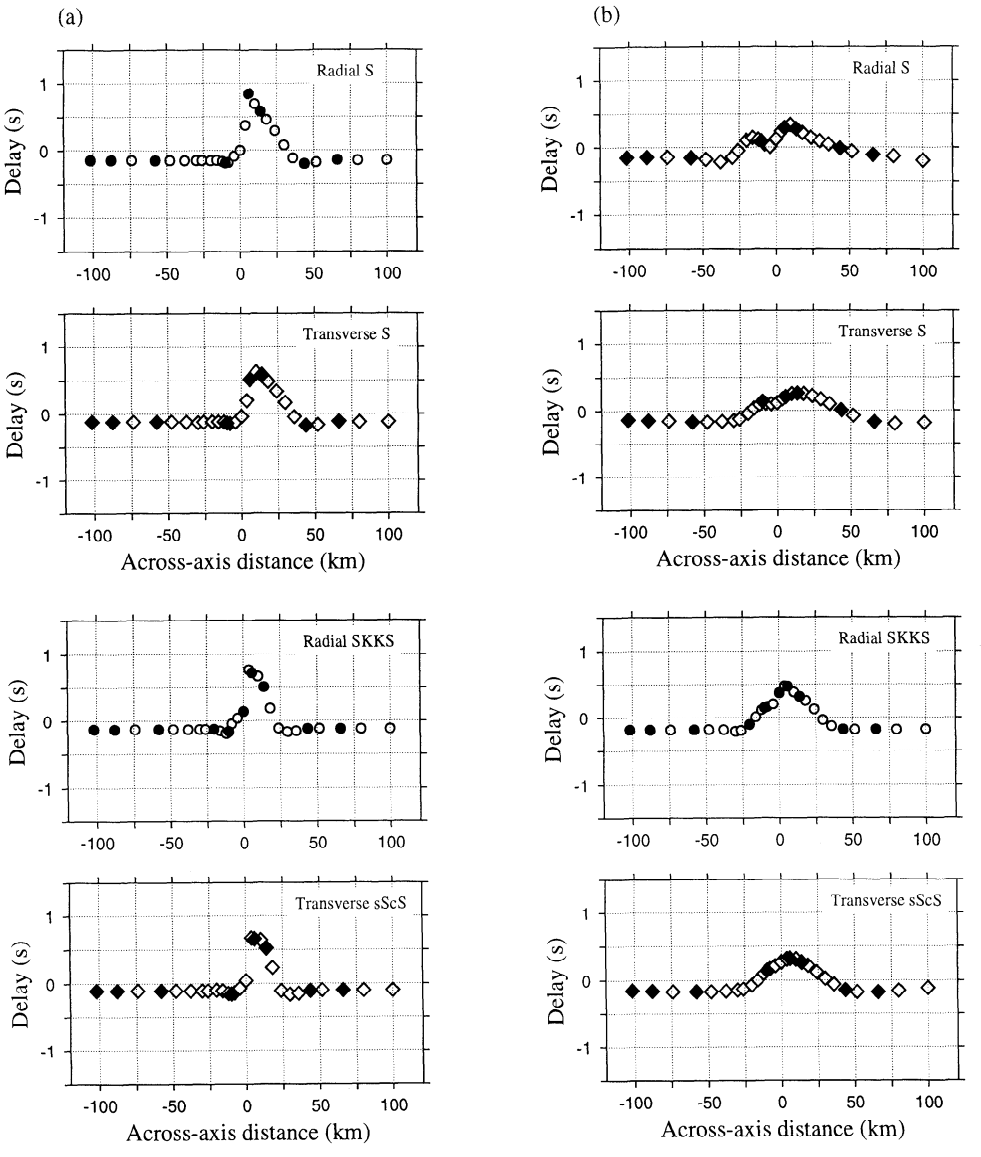

Figure 8. (a) Cross-axis variations of the *S*, *sScS*, and *SKKS* delays predicted from the synthetic waveforms with a dominant frequency centered at 2.5 s. Solid symbols indicate the stations that actually recorded the Tonga or Banda Sea events. The spike-shaped slow anomaly is slightly narrower and closer to the axis for *SKKS* and *sScS* than for the shallower incident *S* arrival. The maximum delay is close to 1 s at station S14 for all the three phases. (b) Cross-axis variations of the *S*, *sScS*, and *SKKS* delays measured from synthetic waveforms that are convolved to have the same frequency content as the observed band-pass-filtered seismograms. The travel time anomaly broadens to some extent, and the maximum delay decreases by a factor of one-third to a half. Although the maximum S delay is reduced to <0.5 s, the *sScS* and *SKKS* phases yield maximum delays at station S14 that are above the detection threshold of the MELT experiment. Both phases provide limits on the scale of the low-velocity zones that can escape notice from the travel time delays.

The peaks on the *SKKS* and *sScS* phases are a little narrower and closer to the axis but should still have a nearly 1-s delay at OBS 14.

The waveforms and delay times are strongly frequency-dependent. To insure that the synthetic waveforms have equivalent frequency spectra to those recorded at the stations, we deconvolve the initial source pulses imposed in wave propagation simulations from the synthetic waveforms, then convolve with the average waveform for each observed phase. The average waveforms are constructed by aligning all the individual waveforms recorded for that phase and stacking. Unfortunately, much of the rich complexity of the waveforms is lost when they have frequency content equivalent to the observed seismograms. Surprisingly, the waveforms become nearly constant across the array (Figures 9 and

10). The minor variations that remain would be difficult to detect in the presence of noise and could not be employed to constrain the shape of the velocity anomaly. However, we still see a strong travel time anomaly that is broadened and reduced in magnitude by roughly one-third to a half depending on the frequencies of the phase pulses (Figure 8b). In terms of detecting an anomaly with an imperfect array on the basis of travel times alone, this broadening may actually be advantageous because, particularly for the *SKKS* and *sScS* waves, it makes it less likely that the delay pattern could lie in a gap between stations.

If the low-velocity zone extends only from 30 to 60 km, the maximum delay is reduced to <0.5 s for both the original and convolved synthetic waves for the 4-km-wide model with 1.0 km/s *S* velocity contrast. The reduction in delay is approximately proportional to the reduction in vertical extent of the anomalous region, so wave front healing during the 30-km propagation from the top of the body to the seafloor has not had much effect on maximum delay times. The higher-frequency waveforms still show characteristic variations from station to station near the axis, but the variability entirely disappears in the observed waveforms with periods longer than 5 s. When the low-velocity zone is 12 km wide, we begin to detect distortion in the lower-frequency waveforms near the axis, but the travel time anomalies are still more robust than the waveform changes. Incidence angle has an important influence on both waveforms and the width of the travel time anomaly, although the maximum delay for *S*, *sScS*, and *SKKS* at observable frequencies is nearly the same, 1.5 s, for the 12-km-wide model conduit with 1.0 km/s velocity contrast.

4. Discussion

The synthetic calculations show that diffraction and wave front healing do not hide the travel time delay signature of a narrow, vertical, low-velocity channel. When such a channel is present, a rich array of reflected and converted waves is generated. The primary

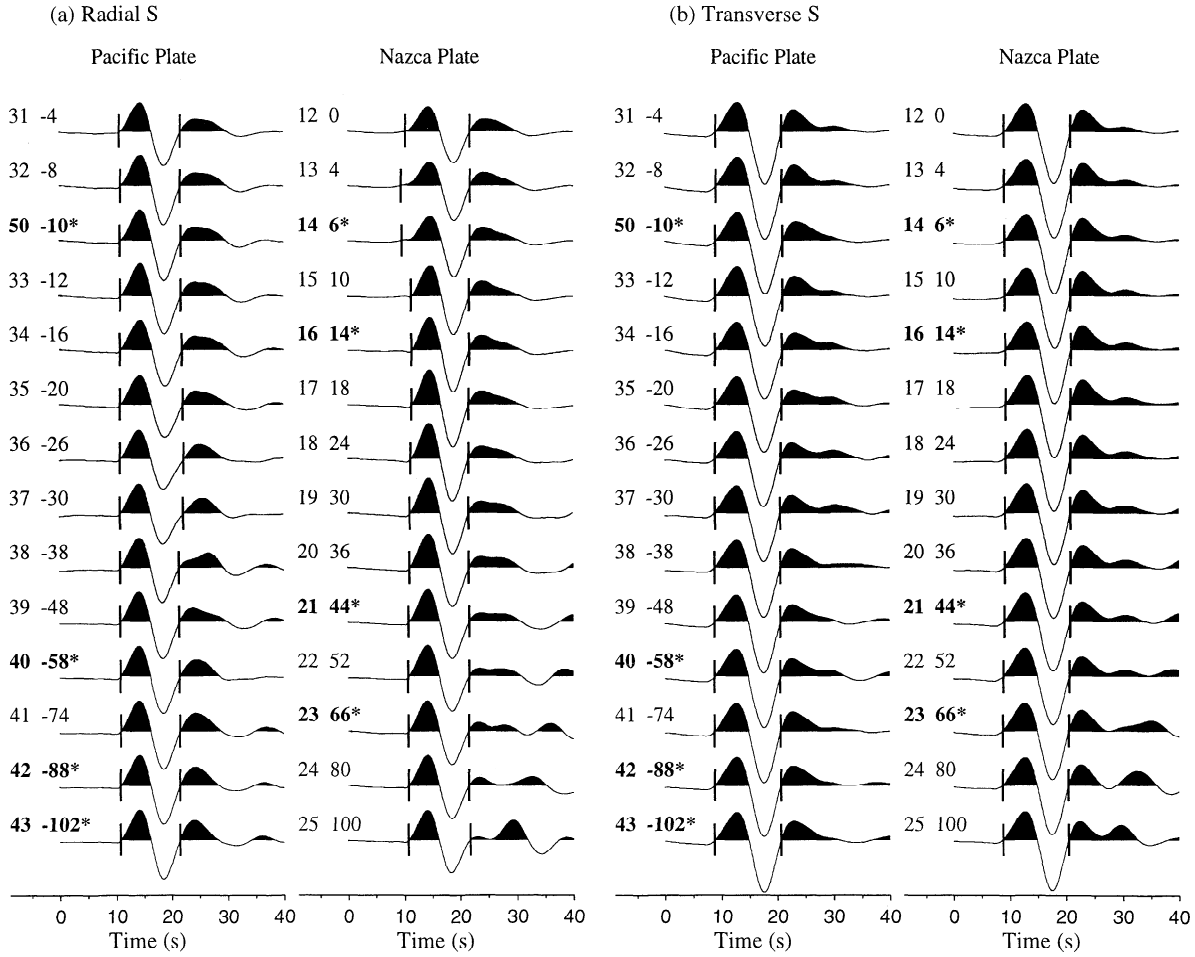

Figure 9. Synthetic *S* waveforms with frequency spectra equalized to the observed seismograms band-passed between 0.03 and 0.15 Hz on the (a) radial and (b) transverse components. The variability in waveform across the array disappears leaving no waveform complexity to indicate the presence of an embedded melt-rich channel.

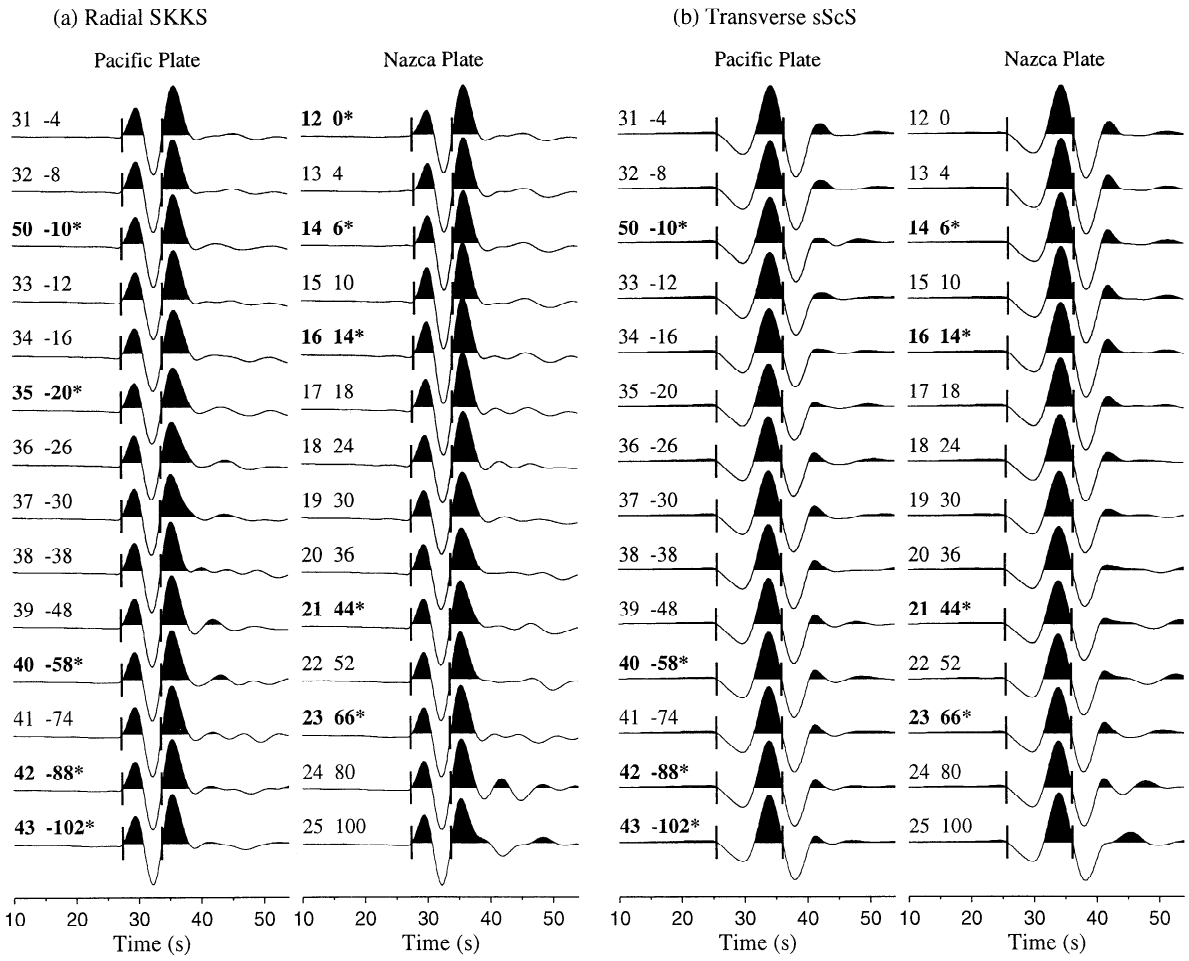

Figure 10. Synthetic waveforms with frequency spectra equalized to the observed (a) radial *SKKS* and (b) transverse *sScS* phases band-passed between 0.04 and 0.2 Hz and 0.03 and 0.15 Hz, respectively. Again the waveforms indicate no observable change across the array.

effects of finite wavelength are to mute the waveform changes associated with these phases. The delay patterns are broadened and decreased in amplitude but are still clearly peaked. The Banda Sea and Tonga events used as examples in this paper generate broad anomalies with no obvious peaks in delay near the axis. Given the scatter in the data, the detection threshold is probably 0.5 s; any anomaly this large or larger would be obvious.

With a threshold of 0.5 s, a 4-km-wide melt channel extending from 10 to 60 km beneath the surface with an S velocity contrast of 1.0 km/s would be detected. Our experiments suggest that such a channel would have to be <2.5 km wide to remain hidden. If the velocity contrast is reduced to ~0.5 km/s, the limit on width is increased to ~5 km. A velocity reduction of 0.5 km/s corresponds to less than 1% melt if the melt is distributed in thin films with an aspect ratio of 0.01, or 5 to 6% if the melt is distributed in tubes along triple junctions [*Forsyth*, 1992]. Taking the distribution of basaltic melt in an experimentally produced ultramafic sample, *Faul et al.* [1994] predict ~3.3% velocity reduction for shear waves per percent melt, which corresponds to 3 to 4% melt for a velocity contrast of 0.5 km/s. *Hirth and Kohlstedt* [1995b] show that the viscosity of the upper mantle may be reduced by an order of magnitude or more if the retained melt fraction exceeds ~4%. *Su and Buck* [1993] show that if several percent melt is retained to provide buoyancy and if the viscosity contrast is more than an order of magnitude, upwelling could be concentrated into a zone of the order of 5 km wide. The viscosity contrast may be enhanced if the surrounding mantle has been depleted of water by the previous extraction of melt [*Hirth and Kohlstedt*, 1995a; *Eberle et al.*, 1998]. Thus it is possible that the threshold, detection limit of the MELT Experiment is just large enough to allow the existence of an narrow, upwelling zone beneath the ridge axis, even though there is no positive, physical evidence that it does exist.

The phase velocities of Rayleigh waves and inversion of waveforms from regional events [*Forsyth et al.*, 1998b; *Webb and Forsyth*, 1998] require that S wave velocities fall below 4.0 km/s in the mantle in a region several hundred kilometers wide. These velocities are so low that they probably require the presence of melt. If there is a background of a small percentage of melt

(~1%) distributed broadly in thin films, it may make it more difficult to detect a zone of higher melt concentration beneath the axis, particularly if that additional melt is concentrated in more equant melt pockets. *Hirth and Kohlstedt* [1995b] point out that melt must be in relatively thick pockets in order to activate the grain boundary sliding mechanism that reduced the viscosity in their experiments. On the other hand, if there is a narrow zone of melt retention and rapid upwelling, then there must be downwelling in the surrounding mantle. Sinking mantle that has released most of its melt to form the crust is unlikely to have any melt in it and would not produce the observed broad zone of low velocities. Thus, although it may be marginally possible to hide a narrow, dynamically upwelling zone within the seismic constraints of the MELT Experiment, it is physically improbable that such a zone exists.

5. Conclusion

Investigation of the seismograms recorded by the MELT OBS network shows that the waveforms are very similar across the array. The delay of the shear waves displays a broad, slow anomaly extending a few hundred kilometers across and gradually decreasing away from the ridge with a larger gradient on the east and the slowest arrival shifted to the west. These observations reveal no evidence for the presence of a narrow zone of focussed upwelling and high melt concentration beneath the fast spreading East Pacific Rise.

General wave theory simulations of *S*, *sScS*, and *SKKS* phases using a pseudospectral method show that a richly complex set of phases would be generated when a narrow, vertical zone of low velocities is encountered. However, this complexity is lost at the relatively low frequencies that can actually be observed, with only the travel time anomalies being retained. Although the travel time anomalies place strong limits on the characteristics of any low-velocity channel and the broad zone of low velocities suggests broad upwelling, the detection threshold is just high enough that a narrow, dynamically upwelling zone of higher melt concentration might escape notice.

Acknowledgments. We thank Yang Shen helping us access the OBS data. Groups led by Spahr Webb, John Orcutt, LeRoy Dorman, Bob Detrick, and John Collins were responsible for collecting the data. Most figures were produced by the GMT software [*Wessel and Smith*, 1991]. The numerical simulations of seismic wave propagation were performed in the parallel SP2 computers at San Diego Supercomputer Center and Center for Fluid Mechanics of Brown University. This research was supported by the National Science Foundation under the grants OCE-9402375 and OCE-9403482.

References

Buck, W. R., and W. Su, Focused mantle upwelling below mid-ocean ridges due to feedback between viscosity and melting, *Geophys. Res. Lett., 16*, 641-644, 1989.

Cordery, M. J., and J. Phipps Morgan, Convection and melting at mid-ocean ridges, *J. Geophys. Res., 98*, 19,477-19,503, 1993.

Eberle, M. A., D. W. Forsyth, and E. M. Parmentier, Constraints on a buoyant model for the formation of the axial topographic high on the East Pacific Rise, *J. Geophys. Res., 103*, 12,291-12,307, 1998.

Faul, U. H., D. R. Toomey, and H. S. Waff, Intergranular basaltic melt is distributed in thin, elongated inclusions, *Geophys. Res. Lett., 21*, 29-32, 1994.

Forsyth, D. W., Geophysical constraints on mantle flow and melt migration beneath mid- ocean ridges, in *Mantle Flow and Melt Generation at Mid-ocean Ridges, Geophys. Monogr. Ser.*, vol. 71, edited by J. Phipps Morgan, D. K. Blackman, and J. M. Sinton, pp. 1-65, AGU, Washington, D. C., 1992.

Forsyth, D. W., et al., Imaging the deep seismic structure beneath a mid-ocean ridge: The MELT Experiment, *Science, 280*, 1215-1218, 1998a.

Forsyth, D. W., S. C. Webb, L. M. Dorman, and Y. Shen, Phase velocities of Rayleigh waves in the MELT Experiment on the East Pacific Rise, *Science, 280*, 1235-1238, 1998b.

Gudmundsson, O., On the effect of diffraction on traveltime measurement, *Geophys. J. Int., 124*, 304-314, 1996.

Hirth, G., and D. L. Kohlstedt, Experimental constraints on the dynamics of the partially molten upper mantle: Deformation in the diffusion creep regime, *J. Geophys. Res., 100*, 1981-2001, 1995a.

Hirth, G., and D. L. Kohlstedt, Experimental constraints on the dynamics of the partially molten upper mantle, 2, Deformation in the dislocation creep regime, *J. Geophys. Res., 100*, 15,441-15,449, 1995b.

Hung, S.-H., and D. W. Forsyth, Modeling anisotropic wave propagation in oceanic inhomogeneous structures using the parallel multi-domain pseudospectral method, *Geophys. J. Int., 133*, 726-740, 1998.

Hung, S.-H., and D. W. Forsyth, Anisotropy in the oceanic lithosphere from the study of local intraplate earthquakes on the west flank of the southern East Pacific Rise: Shear wave splitting and waveform modeling, *J. Geophys. Res., 104*, 10,695-10,717, 1999.

Kennett, B. L. N., and E. R. Engdahl, Travel times for global earthquake location and phase identification, *Geophys. J. Int., 105*, 427-465, 1991.

Magde, L. S., R. S. Detrick, and the TERA Group, Crustal and upper mantle contribution to the axial gravity anomaly at the southern East Pacific Rise, *J. Geophys. Res., 100*, 3747-3766, 1995.

Nishimura, C. E., and D. W. Forsyth, The anisotropic structure of the upper mantle in the Pacific, *Geophys. J., 96*, 203-229, 1989.

Nolet, G., and T.-J. Moser, Teleseismic delay times in a 3-D Earth and a new look at the S discrepancy, *Geophys. J. Int., 114*, 185-195, 1993.

Phipps Morgan, J., Melt migration beneath mid-ocean spreading centers, *Geophys. Res. Lett., 14*, 1238-1241, 1987.

Scheirer, D. S., D. W. Forsyth, M.-H. Cormier, and K. C. Macdonald, The East Pacific Rise and its flanks near the MELT Experiment, *Science, 280*, 1221-1223, 1998.

Scott, D. R., and D. J. Stevenson, A self consistent model of melting, magma migration and buoyancy-driven circulation beneath mid-ocean ridges, *J. Geophys. Res., 94*, 2973-2988, 1989.

Silver, P. G., and W. W. Chan, Shear wave splitting and subcontinental mantle deformation, *J. Geophys. Res., 96*, 16,429-16,454, 1991.

Sparks, D. W., and E. M. Parmentier, Melt extraction from the mantle beneath spreading centers, *Earth Planet. Sci. Lett., 105*, 368-377, 1991.

Spiegelman, M., and D. McKenzie, Simple 2-D models for melt extraction at ridges and island arcs, *Earth Planet. Sci. Lett., 83*, 137-152, 1987.

Su, W., and W. R. Buck, Buoyancy effects on mantle flow under mid-ocean ridges, *J. Geophys. Res., 98*, 12,191-12,205, 1993.

Toomey, D. R., W. S. D. Wilcock, S. C. Solomon, W. C. Hammond, and J. A. Orcutt, Mantle seismic structure beneath the MELT region of the East Pacific Rise from *P* and *S* wave tomography, *Science, 280*, 1224-1227, 1998.

VanDecar, J. C., and R. S. Crosson, Determination of teleseismic relative phase arrival times using multi-channel cross-correlation and least squares, *Bull. Seismol. Soc. Am., 80*, 150-159, 1990.

Webb, S. C., and D. W. Forsyth, Structure of the upper mantle under the EPR from waveform inversion of regional events, *Science, 280*, 1227-1229, 1998.

Wessel, P., and W. H. F. Smith, Free software helps map and display data, *Eos Trans. AGU, 72, 441*, 445-446, 1991.

Wolfe, C. J., and P. G. Silver, Seismic anisotropy of oceanic upper mantle: Shear wave splitting methodologies and observations, *J. Geophys. Res., 103*, 749-771, 1998.

Wolfe, C. J., and S. C. Solomon, Shear wave splitting and implications for mantle flow beneath the MELT region of the East Pacific Rise, *Science, 280*, 1230-1232, 1998.

D. W. Forsyth, Department of Geological Sciences, Box 1846, Brown University, Providence, RI 02912. (donald_forsyth@brown.edu)

S.-H. Hung, Department of Geosciences, Princeton University, Princeton, NJ 08544. (shung@princeton.edu)

D. R. Toomey, Department of Geological Sciences, University of Oregon, Box 1272, Eugene, OR 97403-1272. (drt@mazama.uoregon.edu)

(Received April 9, 1999; revised August 29, 1999; accepted September 8, 1999.)